J. Fluid Mech. (1986), *vol.* 172, *pp.* 401–418
Printed in Great Britain

Flow regimes in a shallow rotating cylindrical annulus with temperature gradients imposed on the horizontal boundaries

By D. H. HATHAWAY AND W. W. FOWLIS
Space Science Laboratory, NASA Marshall Space Flight Center, Huntsville, AL 35812, USA

(Received 19 August 1985 and in revised form 13 May 1986)

The fluid flow types observed in a new rotating cylindrical annulus configuration are presented in regime diagrams. This new annulus has radial temperature gradients imposed on plane, horizontal, thermally conducting endwalls and the cylindrical sidewalls are insulators. This configuration is to be contrasted with the classical cylindrical annulus which has differentially heated conducting sidewalls and insulating endwalls. Studies of the flows occurring in the classical annulus have contributed much to our understanding of basic atmospheric dynamics. Unlike the classical annulus the new configuration permits a measure of control over the internal vertical temperature gradient. To observe the flow from above (and below) and to satisfy the conduction requirement, transparent sapphire disks are used for the endwalls. The fluid used was water. Qualitative observations of the flow types were made using a small amount of rheoscopic concentrate added to the water.

As well as the axisymmetric flow and non-axisymmetric baroclinic wave flow which occur in the classical annulus, two additional non-axisymmetric flow types, boundary-layer thermal convection and deep thermal convection, are observed in the new annulus. Three flow regime diagrams for three different values of the imposed vertical temperature difference are presented. The flows are described and explanations for the flow transitions are offered.

It is argued that the new annulus configuration is more relevant to real atmospheric flows than the original annulus. Another motivation for this research was to provide scientific backup for the Atmospheric General Circulation Experiment (AGCE). The AGCE is a true spherical baroclinic flow experiment which can only be realized in a low gravity environment and which has been proposed for space flight.

1. Introduction

The baroclinic flows generated in a rotating cylindrical annulus with differentially heated sidewalls have been the subject of many experimental and theoretical studies and much is now known about these flows. A detailed review of these studies, which includes many references, has been given by Hide & Mason (1975). The two-dimensional basic states, the transition to baroclinically unstable flow and the steady, finite-amplitude, nonlinear baroclinic waves have been measured experimentally and good agreement found with theoretical predictions (Hide & Mason 1975; Pfeffer, Buzyna & Kung 1980). The annulus flows, and in particular the baroclinically unstable flows, have contributed much to our understanding of baroclinic processes in the atmosphere (Fultz *et al.* 1959; Lorenz 1967).

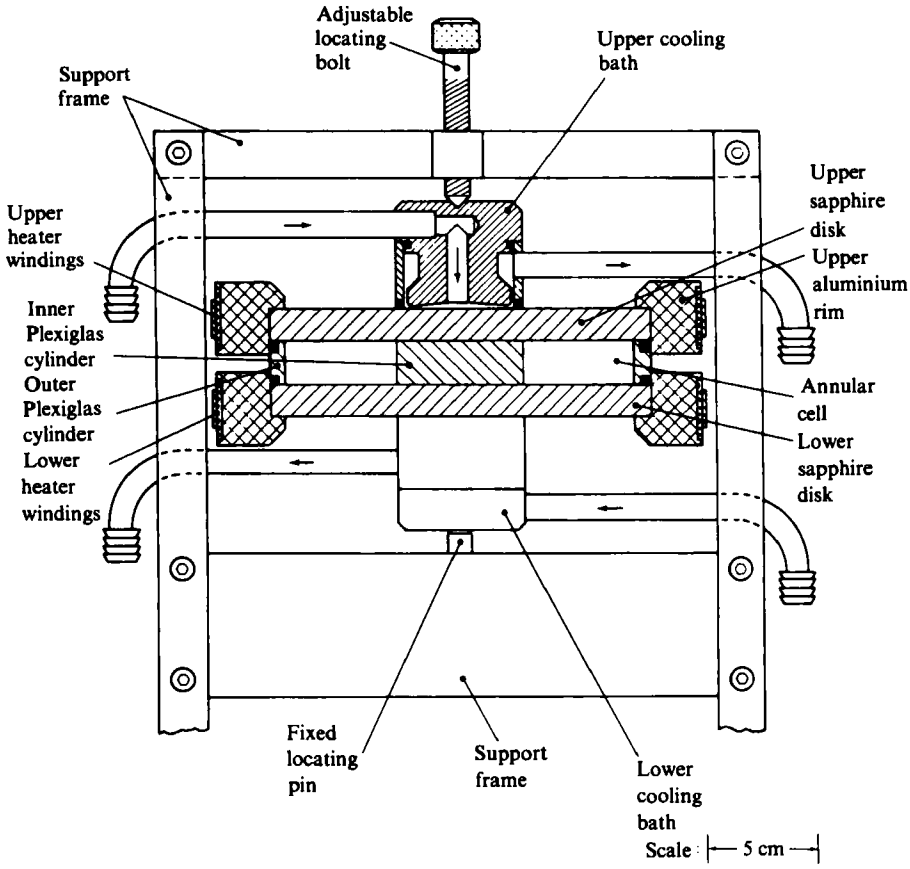

FIGURE 1. The apparatus. This cross-sectional view of the new annulus configuration shows the annular cell bounded by the upper and lower sapphire disks and the inner and outer Plexiglas cylinders. The sapphire disks are heated at their outer edges by heater windings on the aluminium rims. The centres of the disks are cooled by water which circulates through the upper and lower cooling baths. The entire assembly is held level and on axis with the rotating turntable by an aluminium frame which holds the apparatus together by compression.

However, a different cylindrical annulus configuration in which the fluid is subjected to radial temperature gradients on its horizontal boundaries could be more valuable for atmospheric flow studies. This new configuration is shown in figure 1. The imposed temperature distribution permits a measure of control over the vertical temperature gradient (static stability) in the fluid. In the original annulus the static stability depends upon the imposed horizontal temperature difference and the type of flow present and is always stable (positive). In the new configuration the imposed static stability can be positive, negative, or zero. Another advantage of the new configuration is that relatively simple analytical solutions for the basic states (which include heat advection) have been obtained for the infinite plane limit (Hart 1972; Antar & Fowlis 1981). For the classical annulus the only analytical solutions for the basic states are approximations based on boundary-layer theory (McIntyre 1968).

It can be argued that the new configuration is more like the real atmosphere than the original annulus. The atmosphere, like the new annulus, is not heated at a single low latitude boundary and cooled at a high latitude boundary, there is a latitudinal heating gradient. The new apparatus is also shallower than the original with a depth

less than the radial width giving an aspect ratio more like the real atmosphere. (Note, however, that this aspect ratio is still much larger than that for the real atmosphere.) Most experimental studies with the original annulus had a free upper surface. In this matter the new configuration is less like the real atmosphere since a rigid upper boundary is present.

Another motivation for the present study was to provide scientific information for the design of the proposed Atmospheric General Circulation Experiment (AGCE) for Spacelab. A major discrepancy between the laboratory annulus configuration and the real atmosphere is the lack of spherical curvature. The geometry of the real atmosphere is a thin spherical shell not a cylindrical annulus. A true spherical configuration can be achieved in an apparatus flown in an orbiting space vehicle (Giere & Fowlis 1980). Gravity is replaced by a radial dielectric body force obtained by imposing a large voltage across the fluid layer. A study of thermal convection in spherical geometry using an apparatus similar to the proposed AGCE apparatus was flown on Spacelab 3 (Hart *et al.* 1986). The apparatus used for the results presented in this paper is the closest one can come to the proposed AGCE apparatus in an earthbound laboratory.

Some preliminary experimental results for the new annulus have already been presented by Miller & Fowlis (1986). More than one fluid dynamical instability occurs. Four flow types were observed: (i) an axisymmetric Hadley cell flow; (ii) a boundary-layer convective flow; (iii) baroclinic waves; and (iv) cellular convection. Typical examples of these flows are shown in figures 6–9 of this paper.

Miller & Fowlis (1986) presented a single regime diagram for a fluid depth, d, of 1 cm and an imposed vertical temperature difference, ΔT_{V}, of -1 °C (bottom warmer than top). The fluid was water. The axisymmetric flow occurs for relatively large values of the imposed horizontal temperature difference, ΔT_{H}, and for small values of the rotation rate, Ω. Baroclinic instability occurs for higher values of Ω and cellular convection for relatively small values of ΔT_{H}. Boundary-layer convection did not occur for the conditions of the regime diagram but was observed in experiments for other positive values of ΔT_{V}.

Since ΔT_{V} can be varied independently in the new apparatus, the Richardson number can also be varied. A search for symmetric baroclinic instability (Stone 1966; Antar & Fowlis 1983) was performed by Miller & Fowlis (1986) by varying the Richardson number through the range 0 to 1. Symmetric instability was not found.

Results for a similar apparatus have been reported by Koschmieder & Lewis (private communication). In their apparatus a radial temperature gradient is imposed only on the bottom boundary; the upper boundary is isothermal. Axisymmetric Hadley-cell flows were observed and an instability similar to the boundary-layer convection was also observed. Baroclinic instability was not observed.

In this paper a systematic survey of parameter space is described and three new flow regime diagrams for $d = 2.00$ cm and $\Delta T_{\mathrm{V}} = 5$, 1 and -1 °C are presented. In §2 the new apparatus is described. In §3 the experimental techniques and procedures used for this work are described. The regime diagrams and new observations of the flow types are presented in §4. In §5 physical explanations of the observed flow transitions are offered. A summary of the work and conclusions is given in §6.

2. Apparatus

Figure 1 is a simplified scale drawing showing the construction of the new cylindrical cell apparatus. A thermally insulating, solid Plexiglas cylinder of radius $a = 2.54$ cm is located at the centre of the cell. A Plexiglas cylinder of inner radius $b = 6.99$ cm and wall thickness 0.63 cm forms the outer wall. For all of the work reported in this paper the fluid was water and the height of the Plexiglas cylinders was 2.00 cm. The upper and lower boundaries consist of single crystal sapphire disks 1.27 cm thick and 15.24 cm in diameter. Sapphire material was chosen because it is transparent and has a high thermal conductivity ($\chi = 6.5 \times 10^{-2}$ cal/cm^2.s. °C). (This value is close to that of the metal lead.) The transparency allows one to observe the flow and the high thermal conductivity permits an accurate temperature boundary condition. For the maintenance of an accurate temperature boundary condition, the ratio of the thermal conductivity of the boundary material to that of the fluid should be large. For sapphire and water this ratio is 45, whereas for Plexiglas and water the ratio is 0.35.

The sapphire disks were press fitted into the aluminium rims and sealed to provide good thermal contact between the disks and the rims. Each rim was wrapped with resistance heater wire which was connected to a temperature controller. The control sensors are thermistors mounted within brass bolts and screwed into the aluminium rims. The rims and heater windings were constructed to be as azimuthally symmetrical as possible. The temperature control is accurate to ± 0.01 °C. The temperatures of the rims were measured directly using thermistors mounted in the same way as the control thermistors. These thermistors were calibrated periodically using mercury-in-glass precision thermometers (accuracy ± 0.002 °C).

All of the results reported in this paper are for positive radial temperature gradients ($\partial T/\partial r > 0$) on the sapphire disks. Cooling at the centres of the disks is accomplished by water baths mounted onto the outer surfaces of the disks. The diameter of each bath is the same as that of the inner Plexiglas cylinder (5.08 cm). Water from constant temperature circulators flows through the baths and the flowing water is in direct contact with the sapphire material. The temperature tolerance of the circulating water is ± 0.02 °C. The temperature of the circulating water is measured by precision mercury-in-glass thermometers (accuracy ± 0.002 °C) on entering and leaving the water baths. The temperature is higher on leaving each bath because of the radial inward heat flow through the disks. This difference was never more than 0.1 °C and the temperature of each bath was taken as the average of the entering and leaving temperatures.

As a consequence of the cylindrical geometry the steady-state radial temperature profile in the disks is not linear but logarithmic. The non-dimensional temperature distribution is given by

$$\tau = \frac{T(r) - T(a)}{\Delta T_{\mathrm{H}}} = \frac{\ln (r/a)}{\ln (b/a)}, \tag{2.1}$$

where $T(r)$ is the temperature at radius r. Figure 2 is a plot of τ versus r/a for the dimensions of the cell. This temperature profile does not deviate by much from a linear profile.

The Plexiglas cylinders, the sapphire disks and the cooling baths are all held together by simple compression. These items are assembled within a frame (see figure 1). Below the cell assembly and attached to the frame is a vertical tapered pin which fits a matched depression in the centre of the lower bath. The cylinders and disks are aligned with special tools and the threaded pin is screwed downward until the

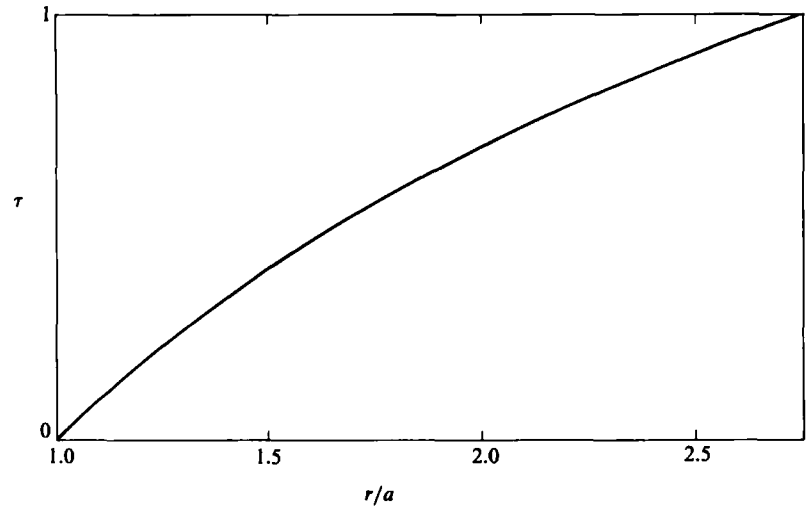

FIGURE 2. The radial temperature profile, τ, as a function of radial position, r/a, on the sapphire disks. For the dimensions of the new annulus this logarithmic temperature profile does not deviate by much from a linear profile.

cell assembly is firmly compressed. The fluid in the cell is sealed by O-rings fitted into the outer Plexiglas cylinder and the water circulating through the baths is sealed by O-rings fitted into the outer rims of the baths.

The frame and cell assembly is mounted on a high accuracy turntable system (a modified Genisco Model 1085). This is a direct drive system (no belts or pulleys) powered by a d.c. torque motor and controlled through a feedback loop using a precision tachometer generator. The rotation rate can be varied from less than 1.7×10^{-3} s^{-1} to 10.5 s^{-1} and the rotational speed stability was always better than 0.1 % of the set rate or 0.01 % of the full-scale output, whichever was greater. Adjustments were made to align the turntable rotation axis and the cell axis of symmetry with the vertical (gravity). The turntable system has electrical slip-rings for power and signal transmission and fluid slip-rings through which the circulating water from the circulators reaches the baths.

To reveal the flow type and structure a small amount of aqueous rheoscopic concentrate (Kalliroscope Corporation) was added to the water in the cell. This substance contains small reflective flakes which align with shear in the flow and, depending upon the direction of lighting and observation, regions of shear appear lighter or darker than the surrounding flow. A circular fluorescent light tube is mounted to the frame below the cell to illuminate the flow. However, for some observations and some flow photographs more contrast was achieved using a light mounted above the annulus or mounted on the side with light passing through the Plexiglas outer cylinder. Since for this research effort we are primarily concerned with recognizing the different flow types, the flow observations are essentially qualitative. However, for strong flows, movement of the flakes could be seen and a few observations of relative flow speed and direction were made. The majority of observations were made from above the cell but a few were also made looking in from the side and from underneath.

We had two strong reasons for choosing the fluid depth to be 2.00 cm. The constraints of the AGCE design (see § 1 and Giere & Fowlis 1980) dictate a depth close

to or less than 2 cm and side observation of the flow is reduced substantially by the aluminium rims for depths less than 2 cm.

3. Experimental techniques and procedures

We can explore a wide range of imposed conditions with this apparatus by varying ΔT_V, ΔT_H, and Ω. The imposed vertical stratification can be made convectively stable or unstable and can vary with radius. However, to keep conditions as simple as possible we kept ΔT_V constant with radius for each individual run. By doing so we also impose the same ΔT_H on the top and bottom boundaries. To keep the gravitational potential surfaces in the cell reasonably horizontal, we limit Ω ($\Omega < 3.73\ s^{-1}$) so that the centrifugal acceleration does not become larger than 10% of the gravitational acceleration.

Our experiments were designed to survey the full range of parameter space accessible with this apparatus. Three sets of experiments were run. Each set was characterized by a different value of ΔT_V, namely, $\Delta T_V = +5$, $+1$, and -1 °C. (The positive sign indicates that the upper boundary is warmer than the lower boundary.) For each set four different sequences were run. Each sequence was characterized by a different value of ΔT_H, namely $\Delta T_H = 2, 4, 10$, and 20 °C. For each sequence several cases were run for different values of Ω in the range $0 < \Omega < 3.49\ s^{-1}$. Where transitions from one flow type to another were found, small steps in Ω were taken to determine the position of the transition boundary more accurately.

Each case was started by rapidly rotating the turntable in alternating directions to agitate the fluid thoroughly and mix the Kalliroscope material throughout the fluid. The turntable was then rapidly spun-up to the desired rotation rate. This procedure gives an easily repeatable experimental set-up. Sufficient time (> 1 h) was then allowed for the flow to settle. The flow type, structure, and time-dependence were then determined by examining the patterns revealed by the Kalliroscope material.

4. The observed flows and regime diagrams

In agreement with the work of Miller & Fowlis (1986), four distinctly different flow types were found with the new cylindrical annulus. Within each of these flow regimes there is considerable variation in the flow structure for different parameter values. Further, although the transitions between most flow regimes are sharp, there is one transition which occurs over a broader region in parameter space. In this section new flow regime diagrams covering a wide range of parameter values are presented. The different flow types are described, new observations are included and explanations for the observed flow transitions are offered.

Figures 3, 4, and 5 are flow regime diagrams for $\Delta T_V = +5$, $+1$, and -1 °C, respectively. The abscissa is the Taylor number,

$$Ta = \frac{4\Omega^2 d^4}{\nu^2}, \tag{4.1}$$

a non-dimensional measure of rotation over viscous damping, where ν denotes the kinematic viscosity of the fluid. The ordinate is the Rossby number,

$$Ro = \frac{\alpha g \Delta T_H}{\Omega^2 (b-a)}, \tag{4.2}$$

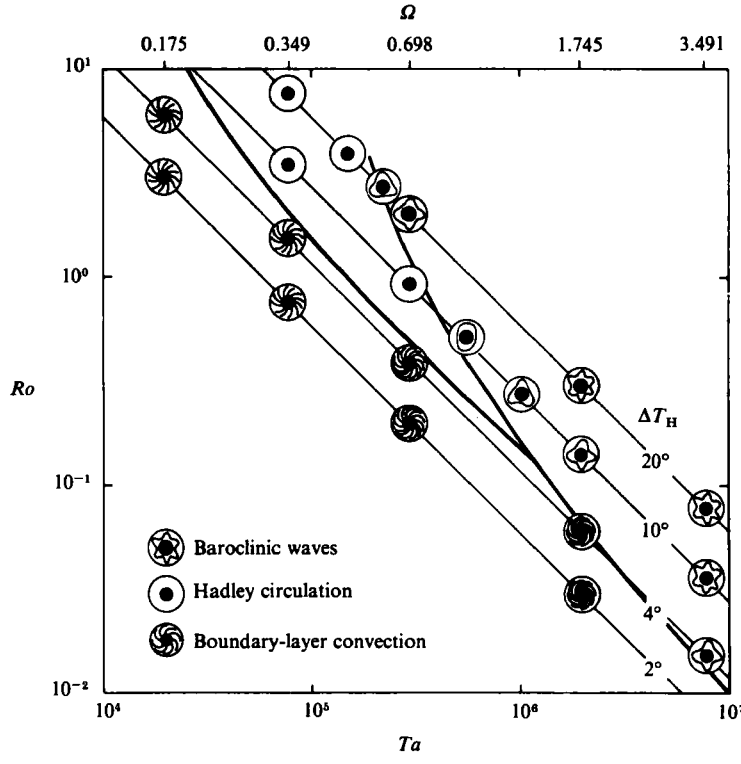

FIGURE 3. The regime diagram for $\Delta T_V = +5$ °C. The abscissa is the Taylor number (Ta) and the ordinate the Rossby number (Ro). The diagonal lines represent contours of constant ΔT_H and are labelled with their respective values. Different flow types are represented by idealized symbols at several representative points and heavy curves are drawn to show the boundaries between the different flow types. Boundary-layer convection occurs for small ΔT_H and for small Ω. Hadley circulations occur for larger ΔT_H and intermediate Ω. Baroclinic waves occur for large ΔT_H and large Ω.

a non-dimensional measure of the horizontal thermal driving over rotation, where α denotes the volumetric coefficient of thermal expansion and g denotes the gravitational acceleration.

Since the annulus geometry and the fluid are not changed for this work and since Ω^2 occurs in both Ta and Ro and the regime diagrams are log–log plots, lines of constant ΔT_H make an angle of 45° with the abscissa and lines of constant Ω are verticals. The symbols used to show the location of experiments in parameter space and the flow type observed should be taken as only idealized representations of the observed flow. Photographs of the flow types at specified parameter locations are included in this paper for detailed study. The transitions between the different flows were found by taking small steps in Ω and are indicated by heavy curves drawn between the flow type symbols. For sharp transitions a continuous line is used and for gradual transitions a broken line is used. Many of the experiments are not represented in the diagrams because of the lack of space available for plotting their positions and because they do not provide any additional information.

Figures 3, 4, and 5 show that for all ΔT_V, for moderate and large values of ΔT_H, and for small values of Ω, an axisymmetric Hadley circulation occurs. Since this circulation can be considered as the two-dimensional basic state for all the observed

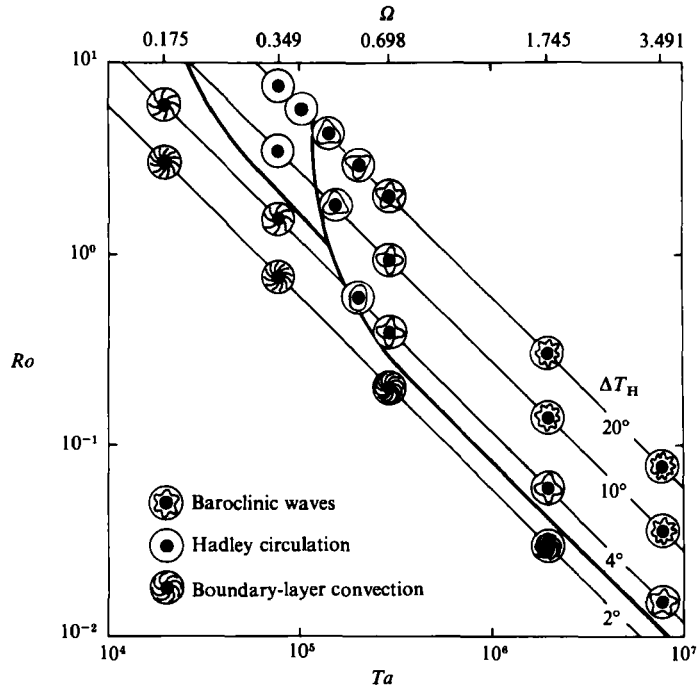

FIGURE 4. The regime diagram for $\Delta T_V = +1$ °C. This diagram is similar to that shown in figure 3 except that the baroclinic-wave regime extends to smaller values of ΔT_H and the flows are more complicated and time-dependent.

instabilities, its characteristics will now be described in some detail. For this discussion we also use the work of Antar & Fowlis (1981) which describes a Hadley cell in a wide rotating, Cartesian channel. A meridional circulation is driven by the temperature gradients on the horizontal boundaries. This circulation is deflected by the Coriolis force and so we also have an azimuthal flow component. For our apparatus the outer radius is warmer than the inner radius and we discuss this specific case. Near the warm outer regions the fluid rises and in the cool inner regions it sinks. Throughout the bulk of the fluid the meridional flow consists only of a radial component confined within the Ekman layers on the top and bottom boundaries. The hot inward flow under the top boundary reduces the imposed vertical temperature gradient in the Ekman layer and can change a positive imposed gradient into a negative one. A similar situation is present for the cooler outflow above the bottom boundary. In the interior the radial flows lead to a corresponding increase of the imposed vertical temperature gradient and can change a negative imposed gradient to a positive one. Our apparatus was always run for counterclockwise rotation and so, consistent with the radial flows, the relative azimuthal flow is in the same direction as the rotation near the top of the cell and has the opposite direction near the bottom. For fixed ΔT_V and Ω as ΔT_H increases, the radial flow increases in strength but remains confined to Ekman layers of fixed thickness. For fixed ΔT_V and ΔT_H as Ω increases, the radial flow weakens and becomes confined to thinner Ekman layers.

Figures 3 and 4 show that for moderate and large ΔT_V, for moderate and small ΔT_H and for the full range of Ω, striations which we identify as boundary-layer convection occur. An example of this flow for $\Delta T_V = +5$ °C and $\Delta T_H = 4$ °C is shown in figure

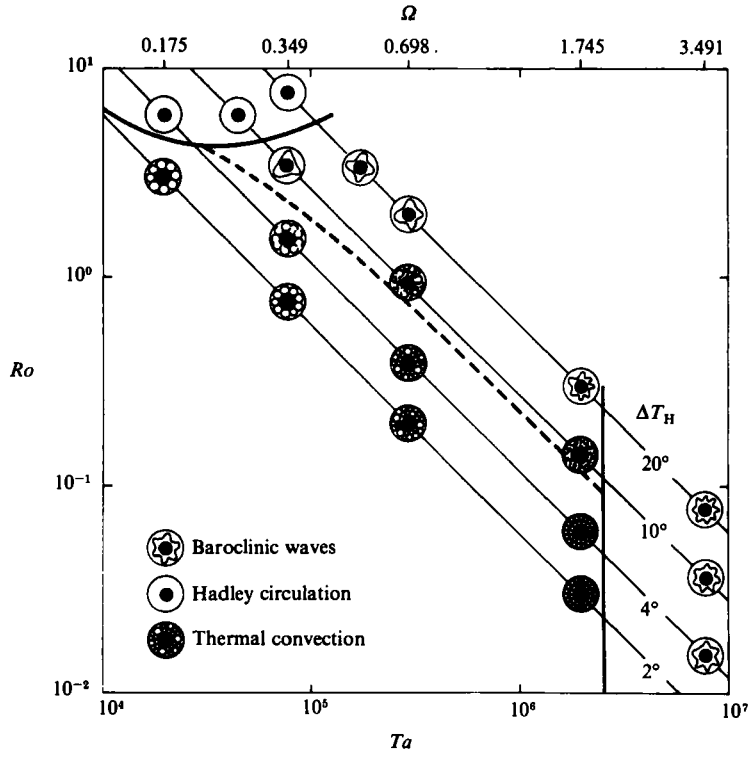

FIGURE 5. The regime diagram for $\Delta T_V = -1$ °C. Deep thermal convection occurs for small ΔT_H except for very large Ω. Baroclinic waves occur for large ΔT_H and moderate to large Ω. For moderate Ω the transition from convection to baroclinic waves is very gradual as ΔT_H is increased and mixed convective/baroclinic instabilities occur. Axisymmetric Hadley circulations occur for moderate to large ΔT_H and for moderate to small Ω. Although not shown on this diagram, boundary-layter convection occurs for $Ta = 0$ at moderate to large ΔT_H.

6. Here, $\Omega = 0$, and the striations are radial. For $\Omega \neq 0$ the striations become curved and for large Ω the striations form a nearly circular spiral pattern. These striations occur near the top surface and near the bottom surface but generally do not extend through the interior of the fluid. They also tend to occur near the inner boundary of the upper surface and near the outer boundary of the lower surface. Since the Hadley cell radial flow can produce negative vertical temperature gradients in the Ekman layers on the horizontal boundaries we believe, following Miller & Fowlis (1986), that the striations are due to thermal instability of the boundary layers. Note that this instability cannot occur in the classical annulus with its thermally insulating horizontal boundaries. The Ekman layers also have strong vertical shear. Simple vertical shear flows have been found to favour convection in the form of rolls aligned with the mean flow (Brunt 1951; Kuo 1963; Deardorff 1965; Ingersoll 1966; Lipps 1971; Hathaway & Somerville 1986). We suggest that the striations of figure 6 show convective rolls aligned with the mean flow.

Figures 3, 4, and 5 show that for all ΔT_V, for moderate and large ΔT_H and for moderate and large Ω, baroclinic instability occurs. In agreement with what was found for the classical annulus, increasing Ω produces more complicated wave patterns and eventually unsteady baroclinic wave flows. Examples of the baroclinic waves are shown in figure 7. In figure 7(*a*), $\Delta T_V = +5$ °C, $\Delta T_H = 10$ °C, and

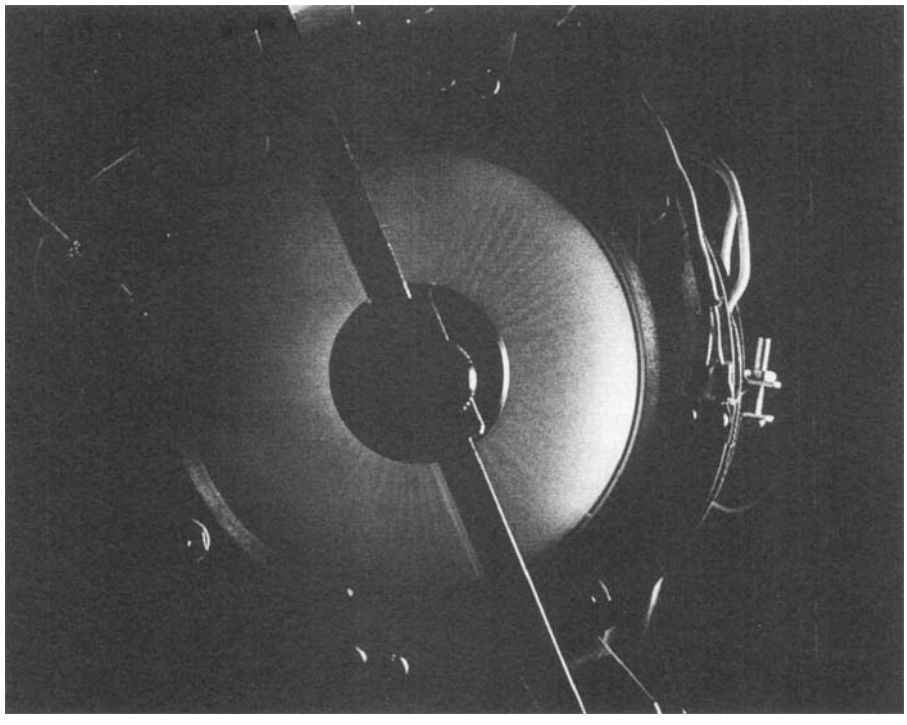

FIGURE 6. The boundary-layer convection observed in the new annulus as revealed by the rheoscopic concentrate. Here $\Delta T_V = +5$ °C, $\Delta T_H = 4$ °C, and $\Omega = 0$. For this non-rotating case the boundary-layer convection forms narrow radial striations which indicate the presence of convective rolls aligned with the boundary-layer flow. For rotating cases the boundary-layer convection forms spiral patterns which indicate the presence of convective rolls aligned with a more azimuthal flow in the boundary layer.

$\Omega = 1.745$ s^{-1} and regular baroclinic waves are formed. The wave pattern carries fluid in a serpentine manner from the warm outer boundary to the cool inner boundary and back. Fronts form between the cold outflow and the warm inflow near the inner radius. Close inspection of these fronts indicates that the fluid velocity abruptly changes direction across the front with flow from the southwest on the warm side of the front and flow from the northwest on the cold side. In figure 7 (*b*), $\Delta T_V = +1$ °C, $\Delta T_H = 10$ °C, and $\Omega = 1.745$ s^{-1} and a realization of more irregular baroclinic waves occurs. A comparison of figures 7 (*a*) and (*b*) reveals that the dominant wavenumber in figure 7 (*b*) is larger and that the flow is much more complicated.

We attempt to explain the observed wavenumber, m, variation in the baroclinic wave regime in terms of the static stability parameter ($S \equiv \alpha g((\partial T/\partial z)/\Omega^2)$). Eady (1949) found for a simple linear model without horizontal shear that as S decreases, progressively larger wavenumbers become the most unstable. For fixed ΔT_V and ΔT_H as Ω increased, m increases. The same result is found in the classical annulus. Increasing Ω under these circumstances weakens the meridional circulation which in turn weakens $\partial T/\partial z$ and both variations decrease S. Thus, the observations are consistent with theory. For fixed ΔT_H and Ω as ΔT_V is decreased, m increases. Decreasing ΔT_V decreases $\partial T/\partial z$ and S, and here the observations are again consistent with theory. A further observation is that for fixed ΔT_V and Ω, as ΔT_H is increased, m increases. The opposite result is observed in the classical annulus. The mechanism of increasing the meridional flow by increasing ΔT_H gives the wrong result. Some other mechanism must be involved in this case.

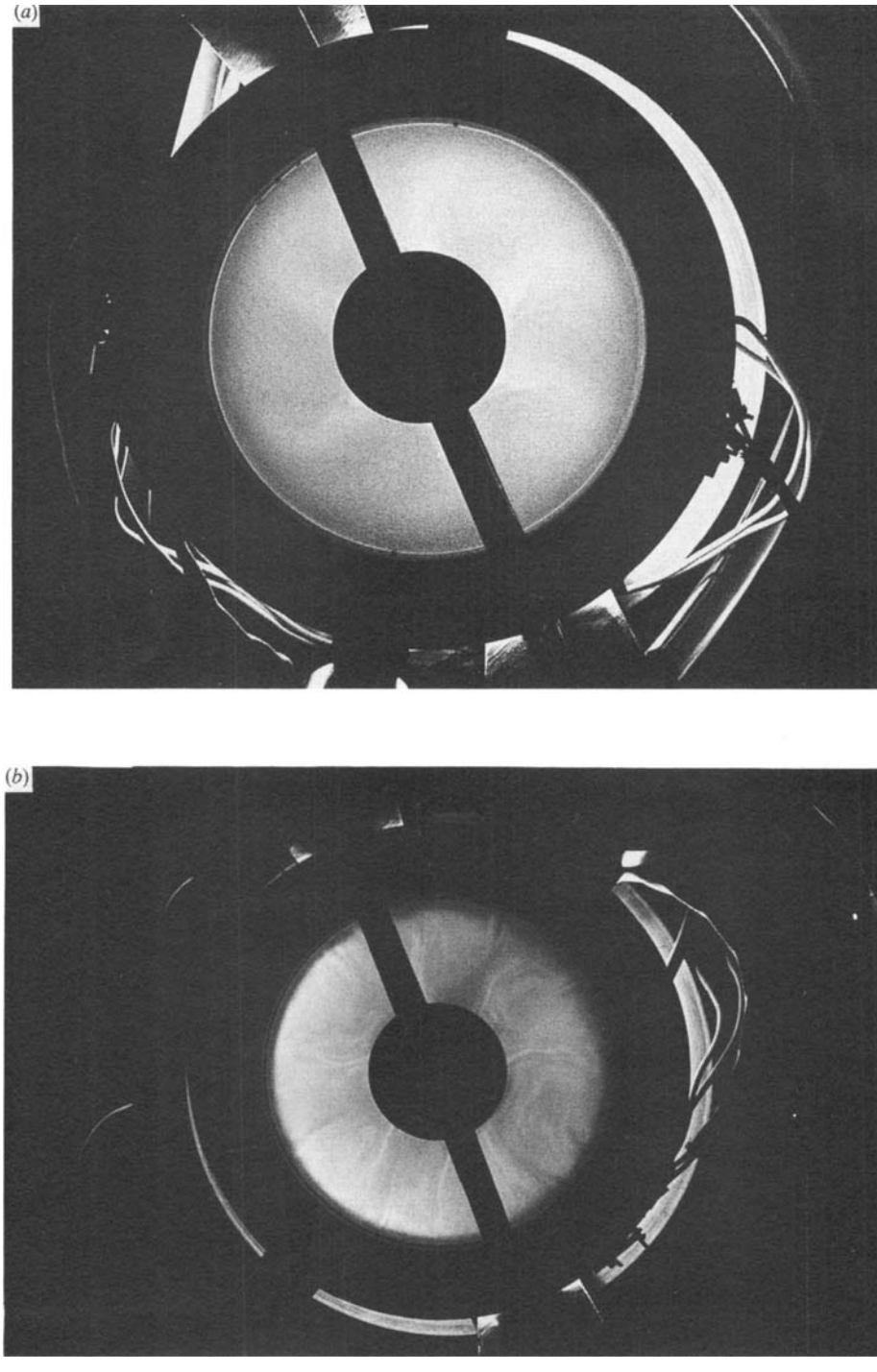

FIGURE 7. The baroclinic waves. In (*a*), $\Delta T_V = +5$ °C, $\Delta T_H = 10$ °C, and $\Omega = 1.745$ s^{-1}. Regular baroclinic waves are produced with a wavenumber of 6. The baroclinic flow carries the fluid back and forth between the warm outer regions and the cool inner regions. Fronts are seen between the cool outflow and the warm inflow near the inner radius. Boundary-layer convection is also faintly visible. In (*b*), $\Delta T_V = +1$ °C, $\Delta T_H = 10$ °C, and $\Omega = 1.745$ s^{-1}. The baroclinic waves are much more complex and have typical wavenumbers of 7 or 8. This flow is also time-dependent.

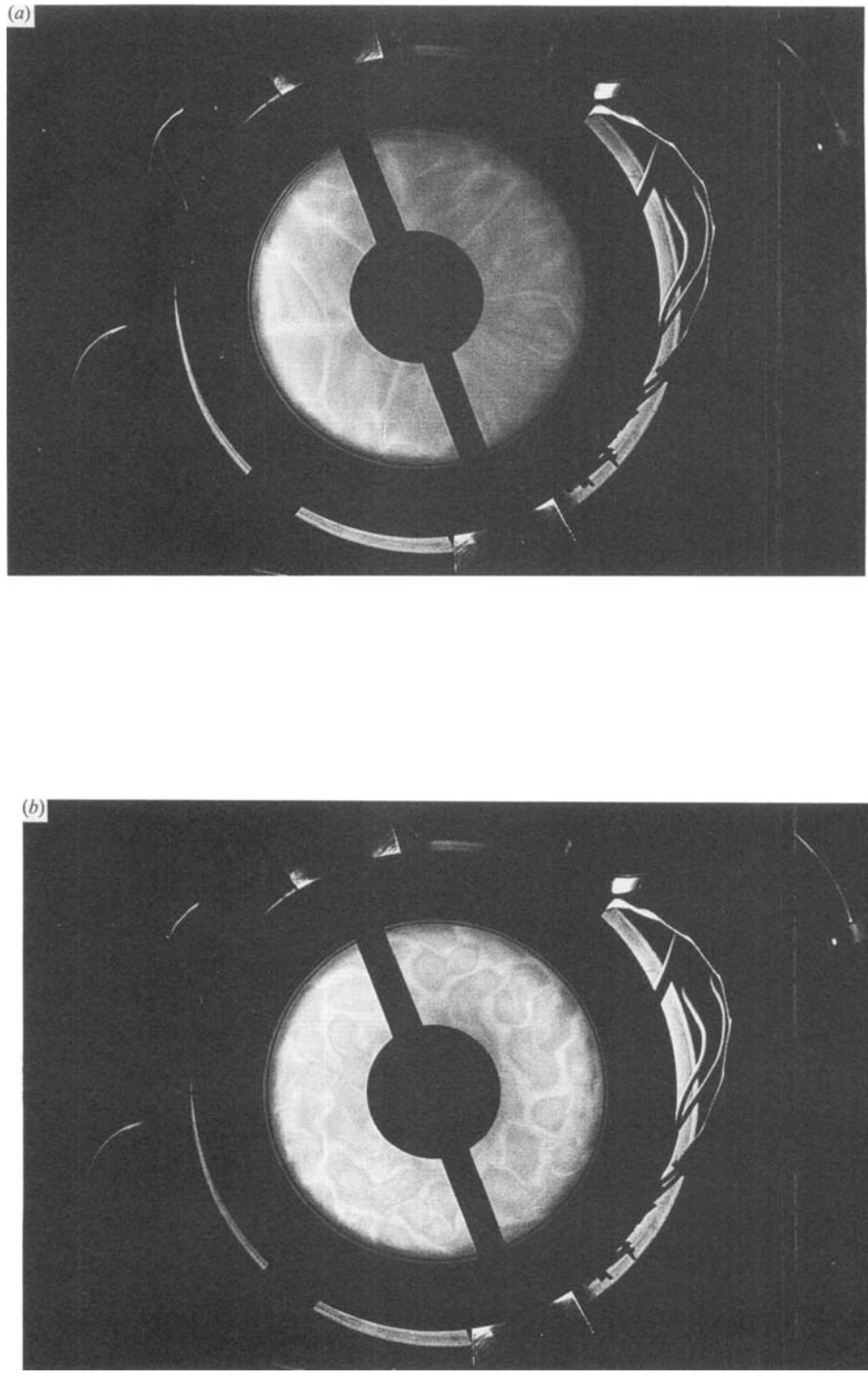

FIGURE 8. The deep thermal convection. In (*a*), $\Delta T_V = -1$ °C, $\Delta T_H = 0$, and $\Omega = 0$. The convective motions span the full depth of the layer and form broad, time-dependent cells. In (*b*), $\Delta T_V = -1$ °C, $\Delta T_H = 0$, and $\Omega = 0.698$ s^{-1}. The convection still spans the full depth of the layer but the rotation produces much smaller cells.

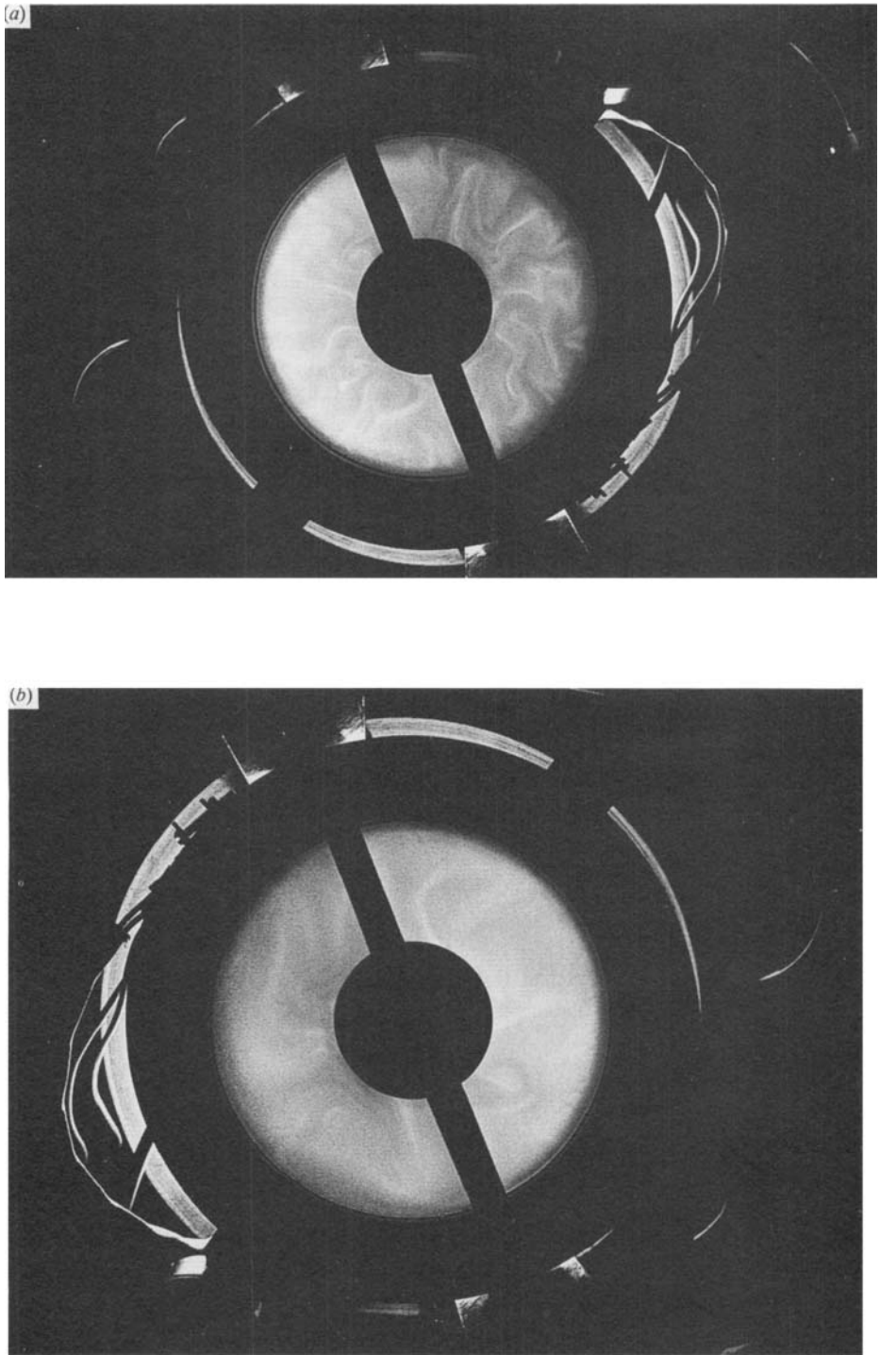

FIGURE 9. The convective/baroclinic eddies. In (*a*), $\Delta T_V = -1$ °C, $\Delta T_H = 10$ °C, and $\Omega = 1.745$ s^{-1}. This very complex and time-dependent pattern shows characteristics of both deep thermal convection (cellular patterns) and baroclinic waves (large-scale horizontal flows). In (*b*), $\Delta T_V = -1$ °C, $\Delta T_H = 10$ °C, and $\Omega = 3.491$ s^{-1} and for this flow the thermal convection characteristics are much less evident than in the more slowly rotating case shown in (*a*).

Figure 5 shows that for negative ΔT_V, for moderate and small ΔT_H, and for a wide range of Ω, thermal convection which spans the full depth of the layer occurs. The Rayleigh number is an important parameter for the onset of thermal convection, it is defined by

$$Ra = \frac{\alpha g \Delta T_V d^3}{\kappa \nu}, \tag{4.3}$$

where κ is the thermal diffusivity. Using the properties of water at 20 °C and taking $\Delta T_V = -1$ °C and $d = 2.0$ cm, we find $Ra = 1.3 \times 10^5$, which is about 76 times the critical Rayleigh number for the onset of convection in a horizontally infinite layer in the absence of rotation and shear (Chandrasekhar 1961). For Rayleigh numbers this large, convection, in general, takes the form of time-dependent, three-dimensional cells (Krishnamurti 1973). Examples of the convection observed in our apparatus are shown in figure 8. Figure 8(*a*), for $\Delta T_H = 0$ and $\Omega = 0$, shows an unsteady, three-dimensional, cellular pattern. As Ω is increased the effect of the Coriolis force is to shrink the horizontal scale of the cells and to form vorticities in the updrafts and downdrafts. Figure 8(*b*), for $\Delta T_H = 0$ and $\Omega = 0.698$ s^{-1}, shows the smaller convection cells.

For moderate Ta as ΔT_H is increased, the convective motions gradually assume the characteristics of the baroclinic waves. This transition is not sharp. Flows in the transition region have a mixed convective–baroclinic appearance. However, for small and moderate ΔT_H as Ω is increased, a much sharper transition to baroclinic waves occurs. Examples of the flows observed on each side of this transition are shown in figure 9. Figure 9(*a*), for $\Delta T_V = -1$ °C, $\Delta T_H = 10$ °C, and $\Omega = 1.745$ s^{-1} ($Ta = 1.96 \times 10^6$), shows a mixed convective–baroclinic flow whereas figure 9(*b*) for the same values of ΔT_V and ΔT_H but for $\Omega = 3.491$ s^{-1} ($Ta = 7.6 \times 10^6$) shows a flow with fewer convective and more baroclinic characteristics.

The results presented in figure 5 for $\Delta T_V = -1$ °C and $d = 2.0$ cm are in qualitative agreement with the regime diagram presented by Miller & Fowlis (1986) for $\Delta T_V = -1$ °C and $d = 1.0$ cm. In both diagrams boundary-layer convection does not appear and regions of mixed thermal convection and baroclinic waves are found.

5. Explanations for the flow transitions

We considered the flow transitions shown in the regime diagrams (figures 3, 4, and 5) and offer the following physical interpretations of the observed results. Note that in figures 3 and 4 the shape of the transition curve from baroclinic waves to the Hadley cell circulation and to the boundary-layer convection is similar to that for the classical annulus for the transition from baroclinic waves to the upper and lower symmetric regimes (Fowlis & Hide 1965; Miller & Gall 1983).

5.1. *The Hadley cell – baroclinic wave transition*

This transition is sharp. The onset of baroclinic instability can be explained in terms of the Eady static stability criterion (Eady 1949). Starting in the axisymmetric regime, as Ω is increased for constant ΔT_H the meridional circulation becomes weaker allowing the internal static stability, S, to decrease. Eady's criterion states that as S decreases, shorter wavelengths become progressively unstable. (In fact, for the Eady model the baroclinic flow in an infinite channel is always unstable since progressively longer wavelengths can always be fitted into the channel.) As soon as a wavelength allowed by the annulus geometry and dissipation in the fluid can grow, the transition occurs. This is also the generally accepted explanation for the

transition from the upper symmetric regime to the baroclinic wave regime in the classical annulus.

5.2. *The boundary layer convection – Hadley cell transition*

This transition is sharp. Starting in the boundary-layer convection regime and increasing ΔT_H for fixed ΔT_V and Ω (see figures 3 and 4), the radial flow in the Ekman layers increases. This, in turn, increases the negative vertical temperature gradient across the boundary layer and increases the shear across the layer. Since a simple shear does not usually lead to stability, we might expect the increased negative gradient to exacerbate the instability. However, the opposite effect is observed. The boundary layer convection gives way to the axisymmetric Hadley cell. Miller & Fowlis (1986) suggested that perhaps the boundary-layer thickness decreases as ΔT_H increases, reducing the value of Ra. This result is not consistent with linear-Ekman-layer theory which predicts a constant thickness for constant Ω. However, this transition does occur for Rossby numbers larger than 1 so that linear-Ekman-layer theory may not be fully appropriate. We suggest that the more complicated Ekman-layer shear, in which the mean flow direction changes with height, leads to stabilization. Asai (1972) has shown that a shear flow that changes direction with height can decrease the growth rates for convective instabilities below the values found for unidirectional shear or in the absence of shear. At present this shear flow stabilization of the boundary-layer convection is mostly conjectural. A more rigorous analysis of the boundary-layer convection needs to be carried out.

5.3. *The boundary layer convection – baroclinic waves transition*

Since this transition is similar in appearance to the lower symmetric–baroclinic waves transition observed in the classical annulus, one is motivated to invoke the explanation for the classical annulus. For the relatively low values of ΔT_H below the transition curve, baroclinic instability processes are unable to overcome damping effects. For larger values of ΔT_H for which baroclinic waves are observed, some traces of boundary-layer convection remain and are faintly visible as striations in figure 7 (*a*). However, the transition to baroclinic waves is sharp.

Although experiments for values of $0 < \Delta T_H < 2$ °C were not performed, we anticipate a transition for $\Delta T_V > 0$ (figures 3 and 4) from the boundary-layer convection regime to a lower axisymmetric flow regime for smaller values of ΔT_H. As ΔT_H is decreased, the radial boundary-layer flow will decrease and so will the negative vertical temperature gradients which drive the boundary-layer convection.

5.4. *The thermal convection – baroclinic waves transition*

Thermal convection was only observed for $\Delta T_V = -1$ °C (figure 5). In this case we have an overall imposed negative temperature gradient and thermal convection is expected. Figure 5 shows that two transitions from thermal convection to baroclinic waves occur. One for fixed Ω and increasing ΔT_H and the other for fixed ΔT_H and increasing Ω. We discuss first the transition for fixed Ω. For small and moderate ΔT_H the radial boundary-layer flow is unable to produce a positive vertical temperature gradient in the interior and so thermal convection occurs throughout the cell depth. However, for large ΔT_H the interior becomes thermally stable and baroclinic waves appear. This transition is very poorly defined. For $\Delta T_H = 20$ °C the flows are definitely baroclinic and for $\Delta T_H = 2$ °C definitely convective, but they appear mixed for intermediate values (see figure 9).

Starting in the thermal convection regime as Ω is increased for fixed values of ΔT_H

a sharp transition to pure baroclinic waves is observed. The linear stability theory for rotating thermal convection predicts a marginal stability curve for which Ra is an increasing function of increasing Ta (Chandrasekhar 1961). For $Ra = 1.3 \times 10^5$ (see §4) the critical value of $Ta = 2.4 \times 10^6$. In figure 5 a vertical line corresponding to $Ta = 2.4 \times 10^6$ was drawn and we find that this line is close to the transition curve between thermal convection and baroclinic waves. Although the theoretical results are for $\Delta T_H = 0$ and for solid-body rotation only, the agreement is good. This result suggests that at least for small and moderate ΔT_H the convection is not much affected by the horizontal temperature gradient. Hathaway, Gilman & Toomre (1979) and Hathaway, Toomre & Gilman (1980) have investigated the onset of thermal instability in rotating layers with both horizontal and vertical temperature gradients. Their analysis suggests that the distinction between convective and baroclinic eddies is vague when $\Delta T_V \approx \Delta T_H$. This is evident in figure 9.

Note for $\Delta T_V = +5$ °C and $+1$ °C that the boundary-layer convection is not stabilized by rotation. This may be due to the fact that the Ekman layers are thin and hence Ta is smaller. In fact, since the Ekman-layer thickness varies as $(\nu/\Omega)^{\frac{1}{2}}$, Ta in the boundary layer is independent of Ω. However, the Rayleigh number across the layer changes, becoming smaller as the layer gets thinner. This suggests that at some larger rotation rate the boundary-layer convection will be stabilized.

5.5. *The Hadley cell – thermal convection transition*

Figure 5 shows a transition from deep convection to the Hadley-cell circulation for small Ta and large Ro. Starting in the upper left-hand corner of the diagram with moderate ΔT_H and small Ω, the strong meridional circulation produces a strong interior static stability which suppresses instabilities and permits a stable Hadley circulation. Decreasing ΔT_H for fixed Ω or increasing Ω for fixed ΔT_H weakens the meridional circulation which weakens the interior temperature gradient. For further changes this gradient changes sign and thermal convection occurs.

Results for $\Omega = 0$ for the values of ΔT_V and ΔT_H, which we cannot show on the regime diagrams ($Ta = 0$, $Ro = \infty$), were also obtained. We found for both $\Delta T_V = +5$ °C and $= +1$ °C with $\Delta T_H = 2$–20 °C and $\Omega = 0$ that boundary-layer convection occurs. This means that the transition between boundary-layer convection and the Hadley-cell circulation shown in figures 3 and 4 continues to bend backwards to the right crossing $\Delta T_H = 20$ °C for small Ta and large Ro. The explanation given for this transition is the same as that already given for the transition for larger Ta and smaller Ro. Starting with very small Ta, the effects of rotation are weak and a simple shear exists in the boundary layer. As we move along a line of constant ΔT_H increasing Ω, the boundary-layer shear becomes more complicated and stabilization results.

We found the following for $\Delta T_V = -1$ °C and $\Omega = 0$. For $\Delta T_H = 2$ °C deep thermal convection occurs. For $\Delta T_H = 4$ °C a mixture of boundary-layer convection and deep thermal convection was observed and for $\Delta T_H = 10$ and 20 °C boundary-layer convection occurs. Thus for $\Omega = 0$ the increased Hadley-cell circulation is able to stabilize the interior for larger values of ΔT_H but not for the smaller values. These results mean that a transition curve between the Hadley-cell regime and boundary-layer convection exists for small Ta and large Ro. For the stabilization of the boundary-layer convection we offer the explanation already given for $\Delta T_V = +5$ and $+1$ °C.

6. Summary and conclusions

Experimental flow regime diagrams have been determined for a new rotating cylindrical annulus configuration which permits a measure of control over the internal vertical temperature gradient. The new configuration reveals more instabilities and flow regimes than the classical annulus and presents the challenge of explaining the observed phenomena. It can be argued that the new configuration is more relevant to atmospheric dynamics studies than the classical annulus.

In agreement with the previous work four flow regimes were observed: (i) an axisymmetric Hadley-cell circulation; (ii) boundary-layer convection; (iii) baroclinic waves; and (iv) deep thermal convection. Three new regime diagrams for fixed geometry and fluid (water) and for $\Delta T_V = +5$, $+1$, and -1 °C are presented. Similar to the flow regime plots for the classical annulus, Ro and Ta are used as ordinate and abscissa respectively, and in the determination of each diagram ΔT_H and Ω were varied. It was found that the transition between all of the regimes occurs abruptly except for the transition from thermal convection to baroclinic waves. This transition takes place over an extended region in parameter space and mixed convection–baroclinic wave flows can be seen clearly.

For the positive values of ΔT_V studied, the shape of the transition curve between the baroclinic waves regime and the axisymmetric flow and the boundary-layer convection is qualitatively similar to that of the classical annulus between the baroclinic waves and the upper and lower symmetric regimes, respectively. The lower symmetric regime is replaced by the boundary-layer convection regime with a new transition between the boundary-layer convection regime and the Hadley cell occurring at relatively small values of Ta and relatively large values of Ro. For the negative value of ΔT_V, the shape of the transition curve between the baroclinic waves regime and the thermal convection regime is qualitatively similar to that for the classical annulus between the baroclinic waves and the lower symmetric regime, except that for the new annulus the transition is not sharp. The transition between the baroclinic waves and the Hadley cell slopes upward for small and decreasing Ta. This is the opposite of the classical annulus result.

Attempts were made to explain the transitions between the flows. The sharp transition for positive ΔT_H from boundary-layer convection to the axisymmetric Hadley cell as ΔT_H is increased for relatively small values of Ta is particularly noteworthy. An explanation based on Ekman-layer shear stabilization is suggested. The contrast between the sharp transition from boundary-layer convection to baroclinic waves (with boundary-layer convection) for positive ΔT_V and the broad transition from deep thermal convection to baroclinic waves for negative ΔT_V is also noteworthy. Perhaps the result that boundary-layer convection can co-exist with the baroclinic waves while deep thermal convection gradually assumes baroclinic aspects will be of interest to atmospheric dynamicists.

REFERENCES

ANTAR, B. N. & FOWLIS, W. W. 1981 Baroclinic instability of a rotating Hadley cell. *J. Atmos. Sci.* **38**, 2130–2141.

ANTAR, B. N. & FOWLIS, W. W. 1983 Three-dimensional baroclinic instability of a Hadley cell for small Richardson number. *J. Fluid Mech.* **137**, 423–445.

ASAI, T. 1972 Thermal instability of a shear flow turning the direction with height. *J. Met. Soc. Japan* **50**, 525–532.

BRUNT, D. 1951 Experimental cloud formation. *Compendium of Meterology*, pp. 1255–1262. Boston.

CHANDRASEKHAR, S. 1961 *Hydrodynamic and Hydromagnetic Stability*. Oxford University Press.

DEARDORFF, J. W. 1965 Gravitational instability between horizontal plates with shear. *Phys. Fluids* **8**, 1027–1030.

EADY, E. T. 1949 Long waves and cyclone waves. *Tellus* **1**, 33–52.

FOWLIS, W. W. & HIDE, R. 1965 Thermal convection in a rotating annulus of liquid: Effects of viscosity on the transition between axisymmetric and non-axisymmetric flow regimes. *J. Atmos. Sci.* **22**, 541–558.

FULTZ, D., OWENS, G. V., BOHAN, W., KAYLOR, R. & WEIL, J. 1959 Studies of Thermal Convection in a Rotating Cylinder with Some Implications for Large-Scale Atmospheric Motions. *Meteor. Monog.* **4**, No. 21.

GIERE, A. C. & FOWLIS, W. W. 1980 Baroclinic instability with variable static stability – A design study for a spherical atmospheric model experiment. *Geophys. Astrophys. Fluid Dyn.* **16**, 207–224.

HART, J. E. 1972 Stability of thin non-rotating Hadley circulations. *J. Atmos. Sci.* **29**, 687–697.

HART, J. E., TOOMRE, J., DEANE, A. E., HURLBURT, N. E., GLATZMAIER, G. A., FICHTL, G. H., LESLIE, F., FOWLIS, W. W. & GILMAN, P. A. 1986 A laboratory model of planetary and stellar convection performed on Spacelab 3. *Science* (In press).

HATHAWAY, D. H., GILMAN, P. A. & TOOMRE, J. 1979 Convective instability when the temperature gradient and rotation vector are oblique to gravity. I. Fluids without diffusion. *Geophys. Astrophys. Fluid Dyn.* **13**, 289–316.

HATHAWAY, D. H. & SOMERVILLE, R. C. J. 1986 Nonlinear interactions between convection, rotation and flows with vertical shear. *J. Fluid Mech.* **164**, 91–105.

HATHAWAY, D. H., TOOMRE, J. & GILMAN, P. A. 1980 Convective instability when the temperature gradient and rotation vector are oblique to gravity. II. Real fluids with effects of diffusion. *Geophys. Astrophys. Fluid Dyn.* **15**, 7–37.

HIDE, R. & MASON, P. J. 1975 Sloping convection in a rotating annulus. *Adv. Phys.* **24**, 47–100.

INGERSOLL, A. P. 1966 Convective instabilities in plane Couette flow. *Phys. Fluids* **9**, 682–689.

KRISHNAMURTI, R. 1973 Some further studies on the transition to turbulent convection. *J. Fluid Mech.* **60**, 285–303.

KUO, H. L. 1963 Perturbations of plane Couette flow in stratified fluid and the origin of cloud streets. *Phys. Fluids* **6**, 195–211.

LIPPS, F. B. 1971 Two-dimensional numerical experiments in thermal convection with shear. *J. Atmos. Sci.* **28**, 3–19.

LORENZ, E. N. 1967 *The Nature and Theory of the General Circulation of the Atmosphere*. Geneva: World Meteorological Organization.

MCINTYRE, M. E. 1968 The axisymmetric convective regime for a rigidly bounded rotating annulus. *J. Fluid Mech.* **32**, 625–655.

MILLER, T. L. & FOWLIS, W. W. 1986 Laboratory experiments in a baroclinic annulus with heating and cooling on the horizontal boundaries. *Geophys. Astrophys. Fluid Dyn.* **34**, 283–300.

MILLER, T. L. & GALL, R. L. 1983 A linear analysis of the transition curve for the baroclinic annulus. *J. Atmos. Sci.* **40**, 2293–2303.

PFEFFER, R. L., BUZYNA, G. & KUNG, R. 1980 Time-dependent modes of behavior of thermally driven rotating fluids. *J. Atmos. Sci.* **37**, 2129–2149.

STONE, P. H. 1966 On non-geostrophic baroclinic instability. *J. Atmos. Sci.* **23**, 390–400.

VERONIS, G. 1959 Cellular convection with finite amplitude in a rotating fluid. *J. Fluid Mech.* **5**, 401–435.